

Fault structure and slip mechanics of the 2022 Mw 6.7 Menyuan earthquake revealed by coseismic rupture observations

Chen Yu^{a,b,c,d}, Zhenhong Li^{a,b,c,d,*}, Chuang Song^{a,c,e}, Bingquan Han^{a,d}, Bo Chen^{a,d}, Xinlong Li^{a,d}, Jianbing Peng^{a,b,c}

^a College of Geological Engineering and Geomatics, Chang'an University, Xi'an 710054, China

^b Key Laboratory of Western China's Mineral Resources and Geological Engineering, Ministry of Education, Xi'an 710054, China

^c Key Laboratory of Loess, Xi'an 710054, China

^d Big Data Center for Geosciences and Satellites, Xi'an 710054, China

^e School of Engineering, Newcastle University, Newcastle upon Tyne NE1 7RU, UK

ARTICLE INFO

Keywords:

Strike-slip faults
Slip surface roughness
Fault bends
Releasing bends
Triangular dislocations

ABSTRACT

Large and shallow strike-slip earthquakes produce striking ground ruptures, damaging roads and infrastructure but providing great opportunities for examining the fault's structure. After the 2022 Mw 6.7 Menyuan earthquake, we observed abundant surface fractures by a combination of optical remote sensing, radar offset and unmanned aerial vehicle measurements. These fractures reveal a complex fault structure including apparent bending geometries and bifurcating branches, which are essential to understanding the mechanisms of faulting. In this paper, we used triangular dislocations to construct the fault geometry that reflected the distribution of measured strike changes but avoided unexcepted discontinuities and overlaps where the fault bent. The modeled fault geometry revealed an extensional releasing bend which was responsible for the southward branching of the fault rupture at its western edge. Our results also demonstrated the potential to explain the occurrence of aftershock clusters and to infer their fault geometries through the correlation analysis of the aftershock distribution and the slip induced stress field. The triangular dislocation model also enabled the calculation of the fault plane roughness and its spatial variation which directly controlled the fault slip magnitude and rupture termination. These analyses reveal an unprecedented level of detail of the fault structure and slip mechanics and, to some extent, offer insights into the physical processes and structural properties of crustal faults in the Earth's shallow crust.

1. Introduction

An Mw 6.7 earthquake struck Menyuan County in the northeast of Qinghai Province, China, on 8 January 2022, causing severe damage to homes and local infrastructure such as the disruption of the Lanzhou–Xinjiang high-speed railway tunnels and the collapse of a section of the Great Wall of China built ~400 years ago. Earthquake parameters from the U.S. Geological Survey (USGS) indicate an epicenter location near (37.828°N, 101.29°E), a focal depth of 13 km, and a sinistral strike-slip dominated mechanism (Fig. 1). 1434 aftershocks were recorded three days following the earthquake, with the largest one measuring Mw 5.1 (Fan et al., 2022). The nearest major earthquake in the region is the 2016 Mw 5.9 earthquake east of the 2022 epicenter. A preliminary study on the source parameters and slip distributions of the 2016 and 2022

Menyuan earthquakes (Li et al., 2022) suggested that the 2016 event generated a substantial positive Coulomb stress change, which might have triggered the 2022 event.

Abundant fault surface ruptures generated by the 2022 Menyuan earthquake were observed on both the Lenglongling fault (LLLF) and Tuolaishan fault (TLSF) spanning ~30 km (Fig. 1a). The most striking feature was the fault trace curvature found on both segments with numerous bends and turns along the faults' strikes, especially the central part of the LLLF, manifesting as a set of disjointed structures. Near its west end, the LLLF forked southward to the TLSF which continued the rupture further west. These non-linear features indicated a set of non-planar fault geometries involved in the rupture which might have a direct control on the fault's slip propagation. Therefore, provided with detailed surface fracture and displacement measurements, this event

* Corresponding author at: College of Geological Engineering and Geomatics, Chang'an University, Xi'an 710054, China.

E-mail address: zhenhong.li@chd.edu.cn (Z. Li).

<https://doi.org/10.1016/j.tecto.2023.230192>

Received 25 November 2022; Received in revised form 3 December 2023; Accepted 20 December 2023

Available online 29 December 2023

0040-1951/© 2023 The Authors. Published by Elsevier B.V. This is an open access article under the CC BY-NC-ND license (<http://creativecommons.org/licenses/by-nc-nd/4.0/>).

offers an opportunity to investigate the slip interaction controlled by the complexity of the fault geometry.

Several previous studies used geodetic observations to investigate the slip mechanics and found considerable slip partitioning along the ruptured faults (Guo et al., 2022; He et al., 2022). They all suggested the rupture was controlled by a complex fault geometry, with Luo and Wang (2022) also speculating that the TLSF might be the continuation of the LLLF. However, the geometric complexities, especially at fault step-overs, joints, and bends, remain poorly understood due to the simplification of the fault geometric model using 2D rectangles and a lack of fault structural observations. These geometric complexities at the Earth's surface reflect the fault structure at depth and may form slip barriers on sliding surfaces (Sathikumar and Barbot, 2021; Xiao et al., 2022). Particularly, Duan and Oglesby (2005) reported that inhomogeneous sliding surface roughness may result in slip heterogeneity. As a result, some of the geometric aspects of the slip mechanics relating to the 2022 Menyuan earthquake are unrevealed or partially studied, notably i) the fault slip propagation and rupture termination, ii) stress interaction and aftershock triggering mechanisms, and iii) the connecting mechanism of the LLLF and TLSF.

To unravel the slip mechanics of the 2022 Menyuan earthquake, we first investigate the detailed fault structure by measuring the earthquake

induced ground fractures. We interpret the fault surface traces using a combination of high-resolution optical remote sensing images (~ 0.8 m), amplitude-based Synthetic Aperture Radar (SAR) pixel offsets and Unmanned Aerial Vehicle (UAV) measurements. We utilize the triangular dislocation model (Comninou and Dundurs, 1975; Meade, 2007; Nikkhoo and Walter, 2015) to ensure a precise co-registration between the measured irregular surface fault traces and modeled fault planes. Using triangular dislocation patches facilitates the study of complex fault geometries (Maerten et al., 2005) and has shown great effectiveness in the investigation of fault segment interactions (Griffith and Cooke, 2004; Olson and Cooke, 2005). We aim to reveal the abovementioned slip mechanics by analyzing the aftershock and stress interaction, the fault branching mechanism and the slip propagation controlled by fault surface roughness. We anticipate these fault structural analysis and slip mechanics contribute to the study of the dynamics of the overall fault systems and the prediction of future earthquake nucleation (Sagy et al., 2007).

2. Geological background

The 2022 Menyuan earthquake initiated on the LLLF in the north-eastern Tibetan Plateau, a tectonically complex region resulting from

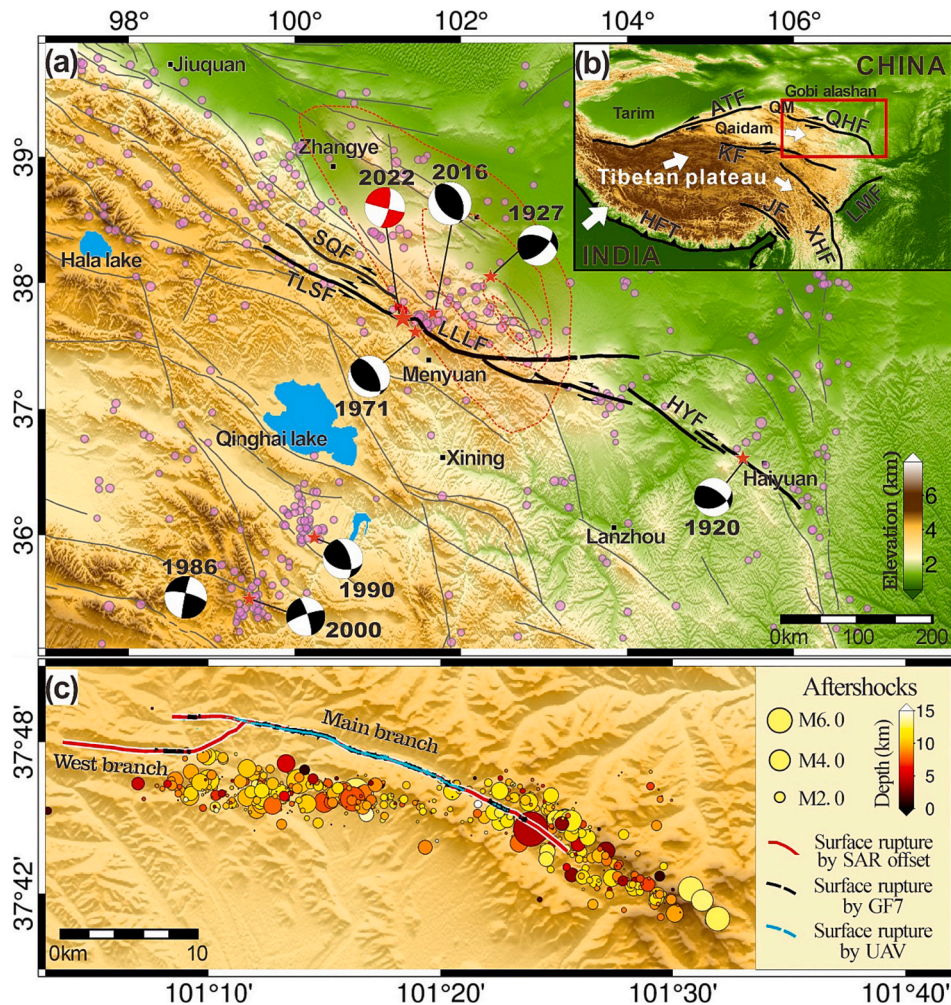


Fig. 1. Tectonic setting around the 2022 Menyuan earthquake (the red beach ball). Focal mechanism solutions for historic events (black beach balls) are from Chen and Molnar (1977); Molnar and Lyon-Caen (1989) before 1986, and from USGS after 1986. Purple dots are background seismicity recorded by USGS from 1990 to 2022. Gray and black solid lines represent mapped faults from the National Earthquake Data Center of China (NEDC, <https://data.earthquake.cn>). Aftershocks are from Fan et al. (2022). LLLF: Lenglongling Fault; TLSF: Tuolaishan Fault; SQF: Sunan-Qilian Fault; HYF: Haiyuan Fault; KF: Kunlun Fault; XHF: Xianshuihe Fault; JF: Jiali Fault; LMF: Longmenshan Fault; HFT: Himalayan Frontal Thrust. (For interpretation of the references to colour in this figure legend, the reader is referred to the web version of this article.)

the intruding of the India Plate beneath the Eurasian Plate. The complexity emerges from the existence of a series of near-rigid blocks such as the Qaidam basin and Gobi Alashan block, causing diverse tectonic settings including sinistral strike-slip faults primarily the Kunlun Fault (KF) and Qilian-Haiyuan Fault (QHF) (Fig. 1b), NNE–SSW crustal shortening such as the formation of the Qilian Mountain (QM), and ESE–WNW extension by normal and conjugate strike-slip faulting. Controversial views remain in literature, owing to accumulated observational evidence established during the past two decades. For example, whether the deformation here was already active with pre-collision shortening at the time of India–Eurasia collision or not until another 10–20 Myr (Yin and Harrison, 2000; Yuan et al., 2013). On the other hand, it is not clear whether the deformation is localized on a number of major strike-slip faults or diffusely distributed throughout the lithosphere (Burov and Watts, 2006; Jackson, 2002). One of the key aspects of answering these questions is to study the structure, layout and slip mechanics of major fault systems in the Earth's shallow crust which are sometimes best revealed by large strike-slip events (i.e., with notable surface ruptures) as is the 2022 Menyuan earthquake.

The LLLF is located in the middle segment of the QHF which exhibits pronounced tectonic deformation and strong seismic activities (Ha et al., 2022). Li et al. (2009) calculated that the average Holocene sinistral strike-slip rate was 4.5 ± 1 mm/yr according to offset geomorphic features and age constraints. Based on Interferometric SAR (InSAR) observations (Huang et al., 2022), the strike-slip rates of the QHF increases from 1.8 ± 0.3 mm/yr in the Halahu segment to 6.4 ± 0.5 mm/yr in the Liupanshan segment. Surrounding the 2022 Menyuan epicenter, frequent medium-to-large events are being recorded notably the southeast 1920 M 8.7 Haiyuan earthquake (Peng et al., 2023; Zhang et al., 1987) and the northeast 1927 Mw 8.0 Gulang earthquake (Gaudemer et al., 1995), with the most recent 2016 Mw 5.9 thrust faulting event 40 km east (Fig. 1) which may have altered the local stress field in favor of the occurrence of the 2022 earthquake (Li et al., 2022).

3. Data

We measured and interpreted the surface fractures (see Data Availability) by a combination of GF-7 optical images (0.8 m resolution), Sentinel-1 SAR offsets (~14 m resolution), Unmanned Aerial Vehicle (UAV) photogrammetric measurements (Table 1). Subsequently, we used triangular dislocations to establish a fault model with irregular fault surfaces.

3.1. High resolution GF-7 optical images

GF-7 optical images were used to determine the spatial distribution characteristic of the surface ruptures. A summary of the available data is shown in Table 1, with data processing performed in the ENVI 5.3 software. First, an orthorectification step was performed on both panchromatic and multispectral images extracted from the GF-7 optical dataset. Second, the Gram-Schmidt Pan Sharpening method was

employed to merge the orthorectified panchromatic and multispectral images (Aiuzzi et al., 2006). Third, pre- and post-seismic GF-7 optical images covering the seismic zone were obtained with a resolution of 0.8 m (Fig. 2).

3.2. UAV digital orthophoto maps

We conducted a field trip after two weeks of the mainshock to investigate the surface rupture patterns generated by the earthquake. We acquired high-resolution images (~5 cm) using the Feima E2000 UAV with 80% forward and 70% sideways overlaps from 27 February to 1 March 2022 (Table 1). Each image was tagged with its geolocation, captured by the on-board Global Navigation Satellite System (GNSS) receiver. The collected data was processed in the Agisoft Metashape software (<https://www.agisoft.com>) which implemented the structure-from-motion (SfM) photogrammetry method (Westoby et al., 2012) to reconstruct the topographic model and the Digital Orthophoto Maps (DOMs).

3.3. SAR displacement measurements

We combined SAR offsets and InSAR phases to estimate the fault slip distribution. Unlike SAR offsets, InSAR phases may lose coherence due to large deformation gradients close to the fault but have an accuracy about one order of magnitude better (Hanssen, 2001). We used two tracks of Sentinel-1 images to form respectively ascending and descending interferograms. The interferograms were generated using the GAMMA software incorporating European Space Agency's precise orbits with the topographic phase contributions removed using the 3-arcsec (~90 m) Shuttle Radar Topography Mission digital elevation model (Farr et al., 2007). To enhance the coherence, we multi-looked the interferogram with a factor of 20 in range and 6 in azimuth and subsequently filtered the interferogram using the weighted power spectrum method. We also estimated and reduced atmospheric phase effects on all the interferograms based on GACOS (Yu et al., 2018). The Line Of Sight (LOS) displacement was then retrieved through unwrapping the interferometric phase with the minimum-cost-flow method (Chen and Zebker, 2000).

Sentinel-1 SAR offsets were processed using the pixel offset tracking technique along the range direction (Michel et al., 1999) following Xu et al. (2018) in the GAMMA software. The offset map can recover large gradient ground deformation (e.g., near-field coseismic areas) at a precision of ~1/20 of the pixel spacing (~0.1 m for Sentinel-1) given a high cross-correlation (Hu et al., 2020), thus exhibiting the fault surface traces clearly as displacement discontinuities.

Note that to take account of the spatial correlation of the densely sampled displacement, we down-sampled the displacement field according to its distance to the fault to allow dense datapoints in the near-field but coarse datapoints in the far field. The ability to measure large deformation by SAR offsets improves the model resolution in the near-field where InSAR loses coherence, whereas the far-field SAR offsets should be excluded due to its low signal-to-noise ratio. In total, we have ~50 k datapoints from InSAR and ~17 k from SAR offsets.

4. Modelling methods

In this section, we first identified the fault surface traces using a set of geodetic observations from which we established a triangular dislocation model to invert for the fault slip distribution.

4.1. The fault surface traces

The precise surface traces were identified through a combination of displacement discontinuities from InSAR phases and SAR offsets, GF-7 images and surface fractures mapped by optimal and UAV images. It should be noted that there are different types of fractures generated by

Table 1

Remote sensing images used in this study.

Data type	Flight direction	Date range	Number of images	Pixel resolution (m) (Range × Azimuth)
GF-7	Orthophoto	20,211,130–20,220,108	2	0.8*0.8
Feima E2000 UAV	Orthophoto	20,220,227–20,220,301	4833	0.05*0.05
Sentinel-1A	Ascending	20,220,105–20,220,117	2	2.3*14
Sentinel-1A	Descending	20,221,229–20,220,110	2	2.3*14

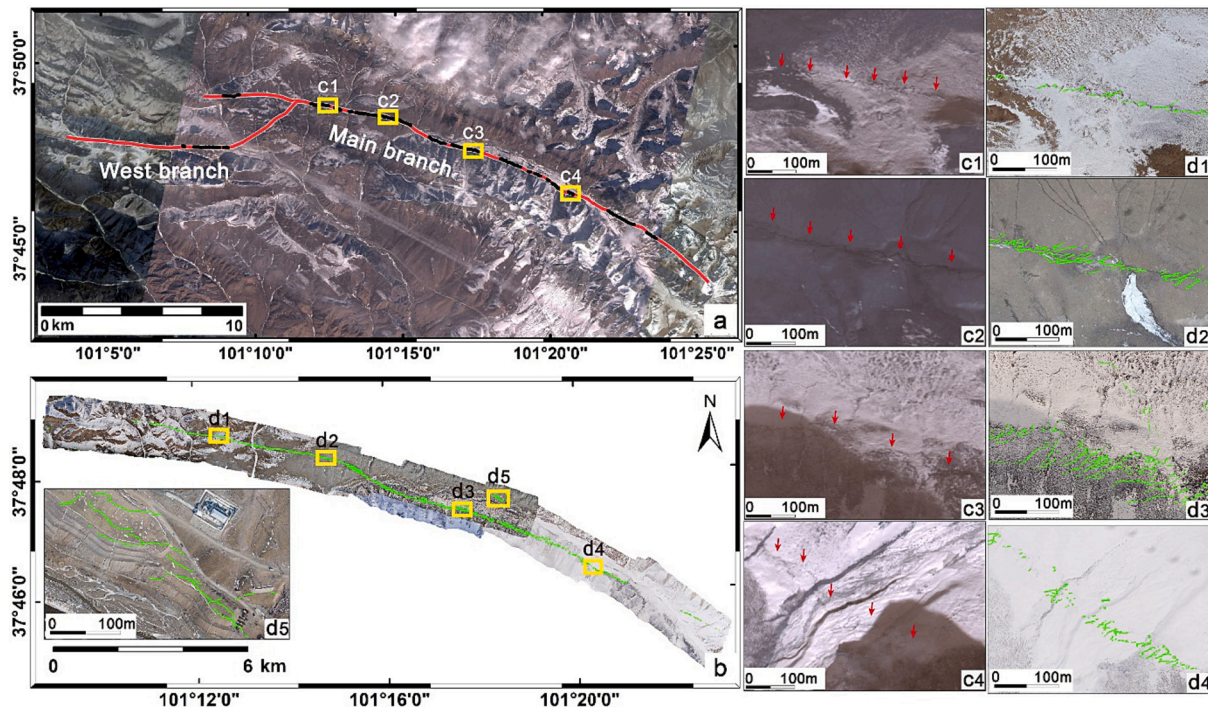


Fig. 2. High-resolution GF-7 optical images and UAV DOMs with identified surface ruptures. Black lines in (a) and green lines in (b) are fault surface fractures interpreted respectively by GF-7 images and UAV DOMs. Red lines are fault surface traces used for modelling and were constructed by a combination of GF-7, UAV and SAR offsets (the same as those in Fig. 1c). c1 to c4 correspond to areas on GF-7 optical images (yellow rectangles) and d1 to d5 correspond to the same areas on UAV DOMs. (For interpretation of the references to colour in this figure legend, the reader is referred to the web version of this article.)

an earthquake, including primary ruptures that generally follow the strike of the main ruptured fault, secondary off-fault fractures (Liu-Zeng et al., 2022), soil failures at nearby landslides (Anastasopoulos et al., 2010) and so on. The purpose of this study is to identify a primary fault surface trace for each fault segment and to establish a dislocation model of ruptured fault planes constrained by the surface traces as will be detailed in Section 4.2.

On GF-7 optical images, the surface fractures generated by the earthquake displayed a darker colour compared to the surrounding area (especially in areas covered by snow, Fig. 2). Based on this feature, we manually extracted a set of linear traces by visual interpretation. For unclear parts where the colour contrast was not significant, we identified fractures by comparing the texture and colour tone variations between the pre- and post-seismic GF-7 optical images. The resultant fault surface traces identified by GF-7 is displayed as solid black lines in Fig. 2a.

On UAV DOMs, fractures displayed similar colour patterns as in GF-7 images but with more details due to the higher spatial resolution. We manually vectorized the edge of the fractures shown on DOMs and recorded its geolocation (solid green lines in Fig. 2b). Fig. 2c and d suggest that the fractures seen on GF-7 and UAV DOMs were in a good agreement, both depicting a curved trace induced by the earthquake. These data are freely available at Section ‘Data Availability’.

On SAR offset and InSAR phase displacement maps, the earthquake generated fractures were manifested as discontinuities which could be used to map the ruptured fault surface trace. We manually interpreted these discontinuities, taking account of also the identified fractures by GF-7 and UAV, especially where the discontinuities became blurred, and determined a primary fault surface traces as shown in Fig. 2a (red solid lines). In general, there was a good agreement among different observations (the disagreement was <300 m), for example, the UAV measured fractures followed exactly the displacement discontinuity observed by SAR offsets near the epicenter.

Some of the identified fractures reflected the surface trace of the ruptured fault plane, but there were numerous off-fault fractures. These

fractures might be caused by earthquake triggered soil failures (Sayab and Khan, 2010) or be related to the fault damage zone extending maximally perpendicularly to the fault by 0.5–1.0 km as observed by UAV (Fig. 2d3 and 2d5). This was a relatively wide zone compared to some documented damage widths such as ~0.1 km along the Punchbowl fault (Chester and Logan, 1986), ~0.2 km along the San Andreas fault at Parkfield (Li et al., 2004), and ~0.3 km along the Landers faults (Li et al., 1998). However, Fialko et al. (2002) investigated the damage along the Calico fault caused by the 1999 Hector Mine earthquake and suggested the observed surface displacement observations were best explained with a 1 to 2 km wide damage zone around the fault. Such a wide zone of off-fault damage might indicate a large cumulative slip on the fault which is roughly positively correlated to the damage zone width (Faulkner et al., 2011).

Two fault branches were identified from the above measured surface fractures namely the main branch and the west branch as shown in Fig. 2a. The main branch extended ~27 km and was far from a straight line but followed a c-shape with numerous turns and bends, reaching an average radius of curvature of 32.9 km. It forked into a west branch near its western end and extended further westward by ~12 km. The west branch had an even larger curvature with a radius of 4.3 km but in the opposite direction against the main branch.

4.2. The fault geometry

To construct a fault geometry that fully reflected the complexity of the measured surface traces, we used a series of finite triangular dislocations in an elastic half-space with a fully analytical solution (Nikkhoo and Walter, 2015). Compared with the rectangular dislocation, the triangular geometry avoids fault patch overlapping and intersecting as the fault plane bends, allowing for a more accurate simulation of curved or rugged fault surfaces. We sampled horizontally a series of vertices at the Earth’s surface along the identified fault traces and also vertically along a fixed dip angle (see below for the determination of the dip angle). The vertices were sampled at a spacing of ~1 km horizontally

and ~2 km vertically at shallow depths, but slightly larger as the depth increased to reduce the number of triangular dislocations at bottom layers (~2 km horizontally and ~4 km vertically at a depth of 20 km). An irregular fault plane consisting of a series of triangular dislocations was constructed by connecting the vertices using the Triangular Irregular Networks (TIN) method (Favalli, 2004). Note that although the vertices were generated according to a fixed dip, the dip of triangles might vary slightly if the fault strike changes, unless the fault dips vertically. As a result, the constructed fault surface shows some degree of irregularities reflecting the changes of the fault strike, i.e., the complexity of the surface fractures.

As the dip angle was unknown, we generated a set of dislocation models using different dip angles, each using the same method described above. We then determined an optimal angle in the slip inversion step as will be detailed in the following section.

4.3. The fault slip distribution

Once the dislocation model was established, we used the displacement measurements to invert for the fault slip distribution on the fault planes. It was considered that the fault slip distribution generally shows some degree of smoothness and a smoothing factor is needed in the inversion to avoid unrealistic slip oscillations (Kaverina et al., 2002; Yabuki and Matsu'ura, 1992). For a 2D fault plane discretized into rectangular patches, the slip distribution can be smoothed by minimizing a Laplacian second-order derivative (e.g., Harris and Segall, 1987). In the case of triangular dislocations, adjacent fault patches may be non-coplanar due to the curvature of the fault plane and a smoothing operator considering fault patch intersections is required. We extended the smoothing operator accounting for forked fault branches described in Jónsson et al. (2002) to the triangular dislocation as follows (Fig. 3a):

$$\|\mathcal{L}\|_2 = \sum_{i=1}^n \frac{(s_i - s_0) \cdot c_i}{d_i^2}, c_i = \frac{\cos(\theta_i)}{\sum_{j=1}^n \cos(\theta_j)} \quad (1)$$

Where \mathcal{L} is a Laplacian operator. d_i and θ_i are respectively the distance and angle between adjacent patches 0 and i . The distance is computed between the geometric centers of the triangles, s_i is the amount of slip on the patch, and c_i is the weight constant that depends on the orientation of the fault patch. Note that there may be more than three adjacent patches for an arbitrary patch if the fault forks into two branches as is in our study. Consider two patches with an angle of θ , when $\theta = 0$, the weight constant $c = 1$ as in the 2D rectangular plane; when $\theta = 90$, the weight constant $c = 0$ and the two patches are

independent (i.e., no smoothing constraint on the two patches). As θ increases from 0, the two patches become increasingly more independent.

The Laplacian operator calculated by Eq. (1) was then introduced in the slip inversion model through a smoothing factor (i.e., a weighting factor) γ (Jónsson et al., 2002),

$$\begin{bmatrix} \mathbf{d} \\ \mathbf{0} \end{bmatrix} = \begin{bmatrix} \mathbf{G} \\ \gamma^2 \mathcal{L} \end{bmatrix} \mathbf{s} \quad (2)$$

Where \mathbf{d} is the displacement observation vector, \mathbf{G} is the green function relating the surface displacements to the fault slip and \mathbf{s} is the fault slip vector.

The slip distribution was then estimated in a least squared sense with a strike and dip component on each of the triangular dislocations. In the meantime, we determined the optimal dip angle and smoothing factor using a grid search method (Feng et al., 2020; Fukahata and Wright, 2008) in which different dip angles ranging from 75 to 90° with a 1-degree step and smoothing factors ranging from 0 to 10 with a step of 0.5 were tested. For each pair of the dip angle and smoothing factor, we constructed a fault geometry with the method described in Section 4.2 and estimated the slip distribution. The optimal values were determined when increasing the slip roughness did not provide significant data misfit reduction (Fig. 3b). We assigned a relative weight between the phase and offset measurements as 10:1 to account for the relatively low accuracy of the latter (Song et al., 2019) and to ensure the datasets were equally well fitted. However, this weight will not significantly affect our estimation as the two kinds of measurements have little overlap, i.e., the offset measurement concentrates in the near-field where the phase measurement losses coherence.

5. Results

5.1. Modeled surface displacements

The observed, modeled and residual surface displacements are shown in Fig. 4. Ascending and descending interferograms showed opposite LOS displacements across the fault zone, suggesting significant horizontal displacements along the fault strike (NW-SE, Fig. 4a1, 4b1). The coseismic deformation from the ascending interferogram showed a dual elliptical pattern with maximum movements of 40 cm and 65 cm toward and away from the satellite, respectively (Fig. 4a1). The descending interferogram revealed a deformation field of 30 × 20 km, with a peak deformation of ~78 cm (Fig. 4b1). Remarkably, the SAR

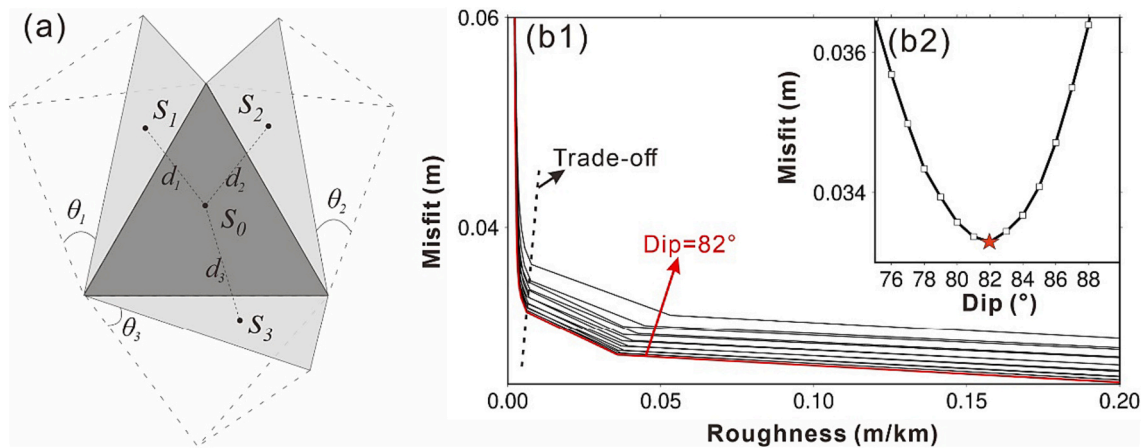


Fig. 3. The determination of the smoothing factor and dip angle. (a) 3D schematic figure of triangular fault patches showing the slip (s_i), distance (d_i , between the geometric centers of the triangles) and angle (θ_i) between adjacent patches. (b) Trade-offs between slip distribution roughness and data misfit using different dip angles and smoothing factors (b1), and between the dip angle and data misfit using different dip angles (b2). The red line indicates slip roughness calculated using the optimal dip angle and the red star in (b2) indicates the optimal dip angle. (For interpretation of the references to colour in this figure legend, the reader is referred to the web version of this article.)

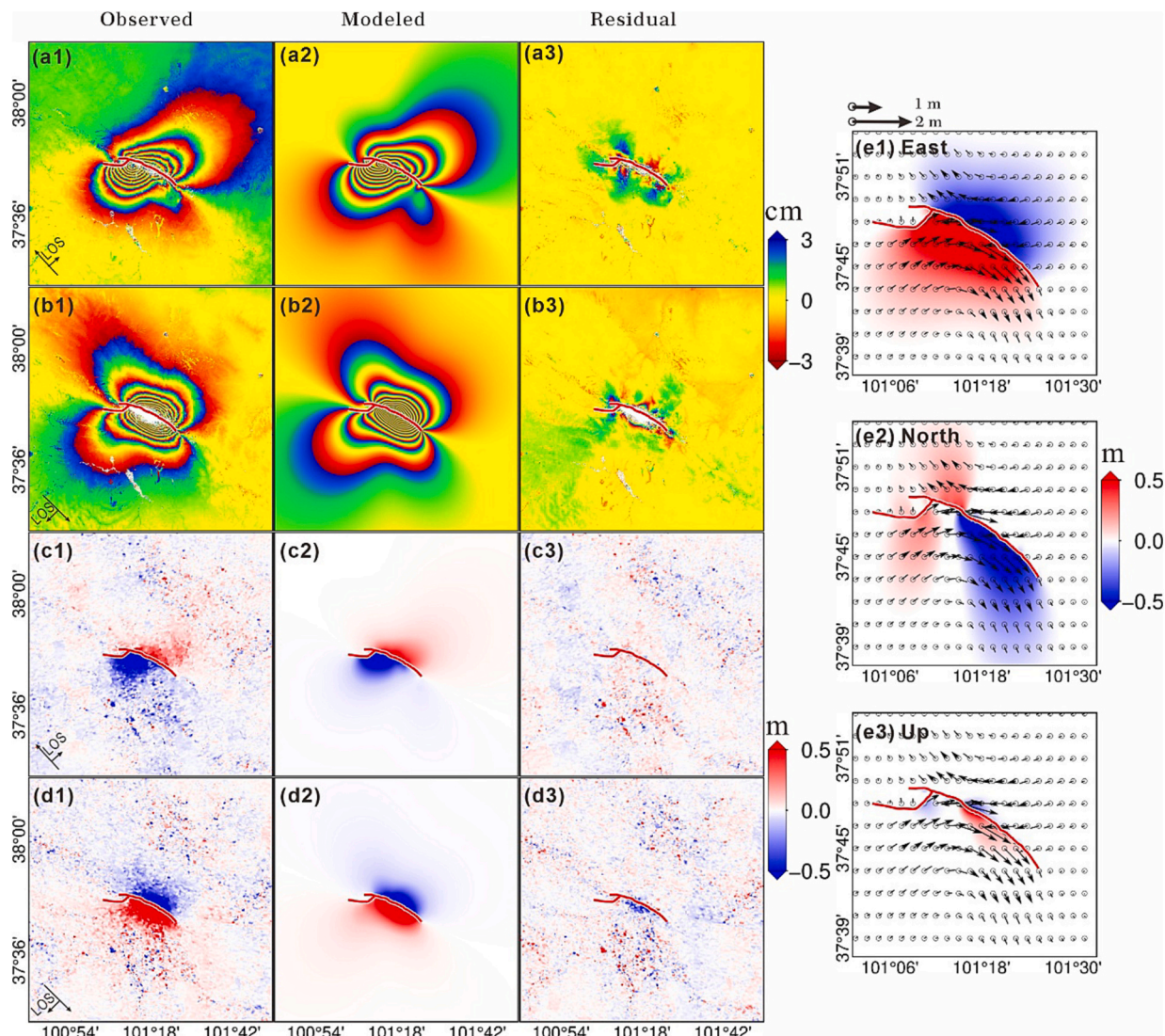


Fig. 4. Observed, modeled and residual surface displacement maps. (a) to (d) are respectively for the ascending surface displacements, descending surface displacements, ascending offsets and descending offsets. (e1 to e3) are the simulated three-dimensional surface displacements, with arrows showing the direction of the horizontal displacements and colour patterns showing the magnitude of the displacement along each direction. Red lines are modeled surface fault traces. (For interpretation of the references to colour in this figure legend, the reader is referred to the web version of this article.)

offset discontinuity on the west branch was also observed on the InSAR interferometric phase maps (Fig. 4a and b) where some degree of coherence was maintained.

We obtained a good agreement with an overall data misfit of 1.1 cm (root mean square between observed and modeled displacements). Some remaining near-fault residuals were considered caused by InSAR decorrelation, unwrapping errors or unmodeled inelastic deformation. Nearly no displacement was observed in the area immediately north of the west branch, possibly because the main fault branch and the west branch generated opposite displacements in the region and therefore canceled each other. Simulated surface displacements showed primarily horizontal components (Fig. 4e1 and 4e2) with minor vertical components (<0.1 m) in the near field (Fig. 4e3). The horizontal displacement field exhibited a considerable rotational effect (black arrows) with a large portion of north-south components at the west and east edges of the main fault branch but mostly east-west components in the middle (Fig. 4e).

5.2. The slip distribution

The resultant slip distribution is shown as 3D plots in Fig. 5. The

2022 Menyuan earthquake was dominantly left-lateral with a small portion of thrusting. The maximum slip reached ~ 4.5 m occurring at a depth of ~ 5 km on the main branch and ~ 8 km east of the bifurcation point. The overall moment magnitude was M_w 6.7 (1.39×10^{19} N·m) and the west branch accounted for 13.6% of the energy release (M_w 6.15).

Fig. 6a shows strikingly that both the main and west surface fault traces generally followed a similar curvature as the nearby mountain ridges, implying that the fault system here was closely related to the regional mountain building process. This might be caused by wide spread compressional zones due to regionally the collision of the India and Eurasia plates. Besides, the fault bends or step-overs might play a role in the mountain building process as seen in the big bend of the San Andreas fault (Cooke and Dair, 2011). We also observed a small portion of thrust slip component ($\sim 11\%$ of the left-lateral component) which might have contributed to mountain formation.

5.3. Aftershocks and the stress field

To investigate the aftershock distribution in detail, we calculated the Coulomb Failure Stress changes (ΔCFS) at a 10-km-depth (the averaged aftershock depth), respectively using the geometry of the main fault

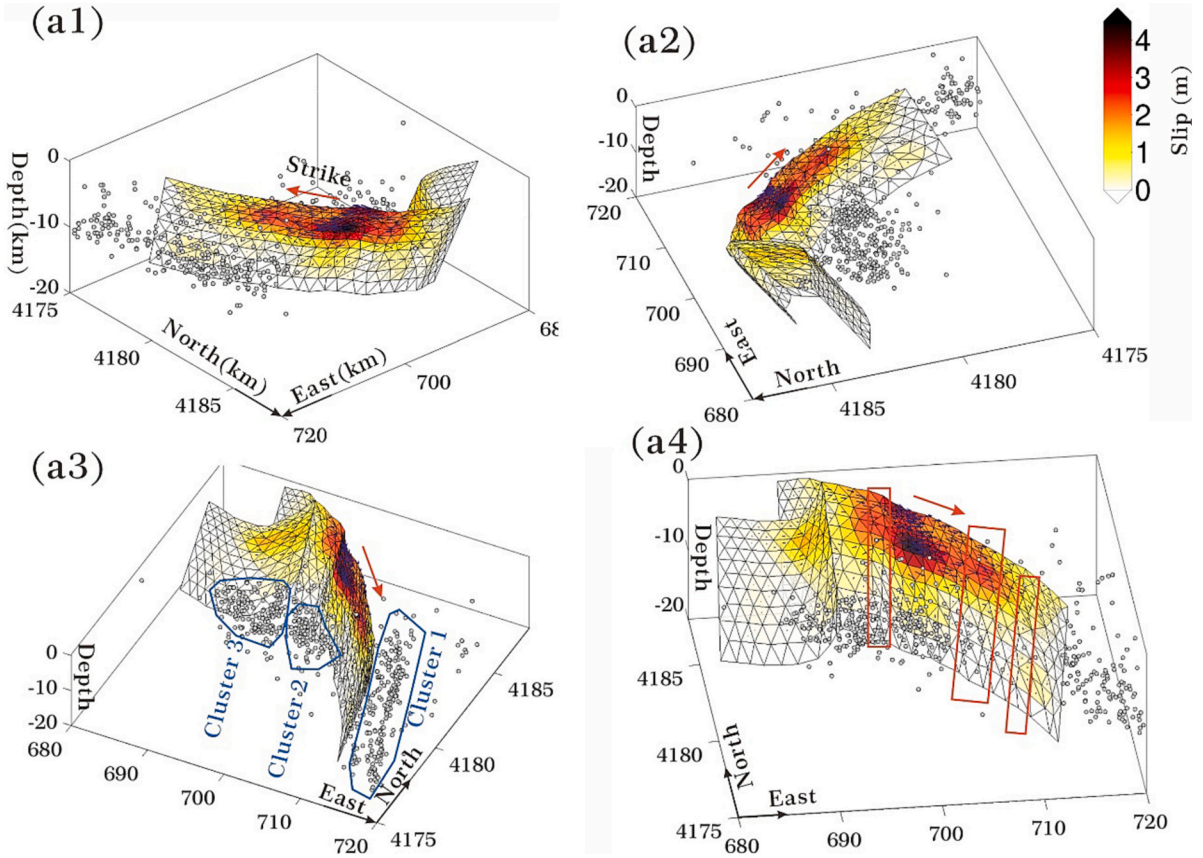


Fig. 5. Fault slip distributions looking from different directions. Gray dots are the relocated aftershocks. Red boxes in (a) show locations where the fault has substantial roughness (see Fig. 7). Blue circles in (a3) show aftershock clusters described in Section 6.1 and Fig. 6. (For interpretation of the references to colour in this figure legend, the reader is referred to the web version of this article.)

branch (Fig. 6c1) and the west branch (the portion immediately connecting the main branch, Fig. 6c2) as the receiver geometries (Toda et al., 2005). Numerous aftershocks were triggered both south and north of the main fault branch and generally below the main slip areas (>7 km). From the east to the west, the aftershocks were firstly parallel to the main fault branch but shifted northwestward by ~ 2 km. The alignment of the aftershock distribution (cluster 1 in Fig. 5a3) implied the existence of an unmapped fault running parallel to the ruptured fault but lacked a connected step-over to enable slip propagation. This might be the remnant of failed or abandoned fault surfaces (Ben-Zion et al., 2003). The loaded stress (>5 bar) here may be partially released by aftershocks or a future earthquake.

The majority of aftershocks occurred in areas with positive ΔCFS (i.e., loaded areas) and the distribution of the aftershocks here were largely controlled by the stress field. These were in favor of the triggering mechanism according to the Coulomb failure criteria (Kilb et al., 2002). Notably, at $\sim 101^\circ 20' E$, the aftershocks were inhibited by a stress shadow (black box in Fig. 6c) and turned southward passing through the main fault branch. Aftershocks did not develop in the stress shadow because the accumulated stress here was already released by the fault slip during the mainshock. Considering the fault geometry, this stress shadow was caused by a sudden change of the fault slip which was inhibited by the fault bend (see Section 6.2 for a more quantitative analysis of the correlation between the bended fault surface and fault slip). Note that such a stress field is hard to retrieve by rectangular dislocation models as the fault bend here would cause overlapping of fault patches, introducing singularities to the stress field.

The aftershocks at cluster 2 were still in a positive ΔCFS zone and approximately parallel to the main fault branch but had a wider distribution than cluster 1. However, going further west close to the west fault

branch, most aftershocks (cluster 3) were found in a negative ΔCFS region, suggesting an inappropriate receiver fault geometry (i.e., the aftershocks were assumed to be on southeast striking faults as was the main branch). However, if the ΔCFS was calculated using a receiver fault geometry the same as the west branch (northeast striking, Fig. 6c2), we can explain nearly all those aftershocks in cluster 3 by positive ΔCFS . This implies that although the aftershock distribution (clusters 2 and 3) south of the main fault branch seemed homogeneous and continuous, depicting roughly a linear structure, their striking directions might have changed from southeast in cluster 2 to northeast in cluster 3. From the calculation of ΔCFS using different receiver fault geometries, we can also locate a narrow transition zone which occurred at $\sim 101^\circ 13'$, ~ 4 km east of the fault bifurcation point (the gray box in Fig. 6c2).

Our results reveal a remarkable relationship between the aftershock distribution and the slip induced stress field. Furthermore, according to the Coulomb failure criteria, we can infer the fault geometry of aftershocks by investigating the distribution of ΔCFS which is an effective procedure to predict aftershock mechanisms. This is essential for assessing seismic hazards, improving earthquake forecasting, and advancing our understanding of the overall earthquake behavior.

6. Discussion

6.1. Why the fault forked southward to the TLSF?

The type of the fault bend has long been considered crucial in determining strike-slip rupture propagation and extent (Langridge et al., 2002). By investigating the detailed fault surface ruptures of the 2022 Menyuan earthquake, we identified the portion on the west branch

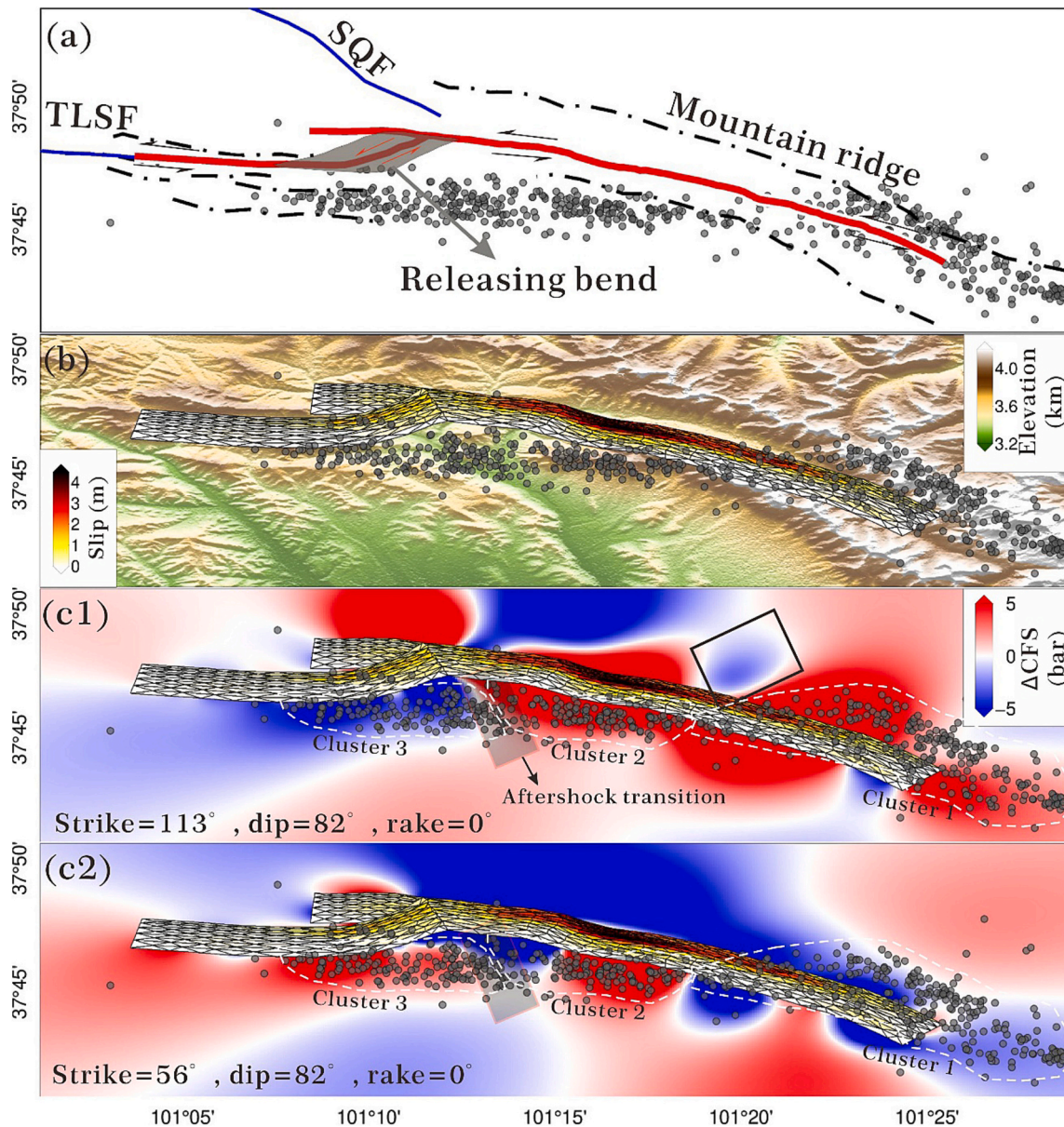


Fig. 6. Fault slip projected onto the Earth's surface and ΔCFS . Dotted lines in (a) are mountain ridges from topographic data. Blue lines are mapped faults from NEDC. TLSF: Tuolaishan Fault. SQF: Sunan-Qilian Fault. The assumed receiver fault orientation for the ΔCFS calculation is the averaged main fault branch in (c1) and the west fault branch in (c2). The gray boxes in (c) marked the transition location where the fault geometry of aftershocks has changed. (For interpretation of the references to colour in this figure legend, the reader is referred to the web version of this article.)

immediately connecting the main branch as geometrically a releasing bend, deviating $\sim 45^\circ$ from the main fault branch (Fig. 6a) and accommodating extension induced by the faults' left-lateral slip. Through this releasing bend, the fault forked southward to the TLSF, rather than northward to the SQF (i.e., requiring a restraining bend and both the TLSF and SQF were close enough to transfer slip). This is because firstly, releasing bends produce pull-apart basins which are different from restraining bends where push-up ranges may be formed. As extensional normal stress promotes plastic yield as opposite to the compressive normal stress in the upper crust (Ye et al., 2015), a releasing bend has stronger strain localization and is easier to form than a restraining bend (e.g., Li and Zhou, 2018). Furthermore, numerous restraining bends were found to have acted as rupture terminations, such as at the Aksay bend of the Altyn Tagh Fault (Elliott et al., 2015), the Akyazi Bend of the north Anatolian fault zone (Langridge et al., 2002) and a restraining bend at the northwestern edge of the Coyote Creek fault (Allen et al., 1968). Therefore, the number of ruptured releasing bends is generally

much higher than that of restraining bends (nearly 3–6 times more) along major strike-slip faults (Mann et al., 2007; Wesnousky, 2006). As the rupture propagated away from the epicenter, the fault slip decreased, and the overall rupture energy near the west branch was insufficient to cross the restraining bend required to connect to the SQF. Instead, it succeeded in spreading through a releasing bend to the TLSF which was perhaps already at its rupture tipping point. In terms of the frictional property, there might be more frictional resistance at the NW end of the main fault branch due to decreased slip velocity in a slip-weakening regime (Sone and Shimamoto, 2009) or less historic cumulative displacements, compared to the west branch, given the fact that slip occurs more easily on old rupture surfaces than on fresh fractures (Andrews, 1989).

Branched fault ruptures are frequently observed on major fault systems in the Tibet plateau such as the 2008 Wenchuan earthquake (Shen et al., 2009), the 2017 Jiuzhaigou earthquake (Zheng et al., 2020) and the 2021 Maduo earthquake (Pan et al., 2022). The abovementioned

approach to investigate the branching mechanisms utilizing detailed fault structural information may provide new insights for future earthquake nucleation of nearby faults and the generation of regional seismic hazard maps.

6.2. Slip magnitude and fault surface roughness

Roughness of a fault's surface evolves with the fault maturation, with cumulatively small-slip faults being rougher than large-slip faults due to the consolidation of multiple fault structures during slip (Sagy et al., 2007). Therefore, variations of cumulative slip along a fault result in heterogeneous roughness which is a key controlling element of the earthquake nucleation, growth, and termination. Utilizing the triangular dislocation model, we are able to calculate the roughness of the fault segments ruptured in the 2022 Menyuan earthquake which is however difficult when using rectangular dislocations due to unexpected overlaps and discontinuities when the fault's strike and dip changes. To quantify the fault roughness, we defined a simple roughness indicator for each triangle which was the averaged angle between the triangle and all its neighboring triangles (Fig. 3a). A small angle indicated a smooth surface (i.e., close to a flat plane), and a large angle indicated a rough surface (i.e., a concave and convex surface). Such a direct calculation of the fault surface roughness is rare in literature as observations on fault surfaces are difficult to acquire and most previous studies used synthetic simulations (e.g., Tal et al., 2020) or in house experiments (e.g., Fryer et al., 2022). We should make it clear that the fault surface roughness in this study was geometrically determined from the observed surface rupture traces, and it only reflected the fault bending and turning along the Earth's surface. Therefore, the direction of the calculated roughness was

essentially along-strike. To calculate the along-dip roughness, in-depth measurements constraining the fault dip would be required.

Most of the fault slip occurred in smooth areas with a roughness less than $\sim 2^\circ$ and the roughness played an important role in slip propagation and termination. Areas with substantial roughness were found at fault bends on both fault branches (e.g., red boxes in Fig. 7a). Fig. 7b compares the along-dip cumulative slip and mean roughness at every location along the fault strike. The major slipping patches were surrounded by two bends with considerable surface roughness, resulting in sharp decreases of the slip when propagating sideways. Without the bends, the slip profile in Fig. 7b would decrease more gradually forming a wider distribution such as those observed by Dawers et al. (1993). Slip increased slightly after passing through the bend on the right (east) of the major slipping patches, but decreased sharply before crossing the second bend in the east. Noticeably, slip decreased immediately when arriving at the edges of bends, rather than reaching the peak area of the surface roughness. These slip and fault surface roughness correlations suggest that fault bends acted as barriers impeding slip propagation and even a small change of the fault surface roughness can cause significant slip drop. Therefore, the fault surface roughness caused by fault bends has a direct control on the homogeneity of the slip distribution and thus the earthquake magnitude.

As the fault slip model used above was inverted simultaneously with an optimal smoothing factor (3.5), it is worth investigating its impact on the relationship between slip distribution and fault surface roughness. We inverted for two additional slip models (by fixing the dip angle to the optimal value as in Section 4.3 and Fig. 3), an under-smoothed slip model with a smoothing factor of 0 (Fig. 7c1) and an over-smoothed slip model with a smoothing factor of 10 (Fig. 7c2). A comparison between

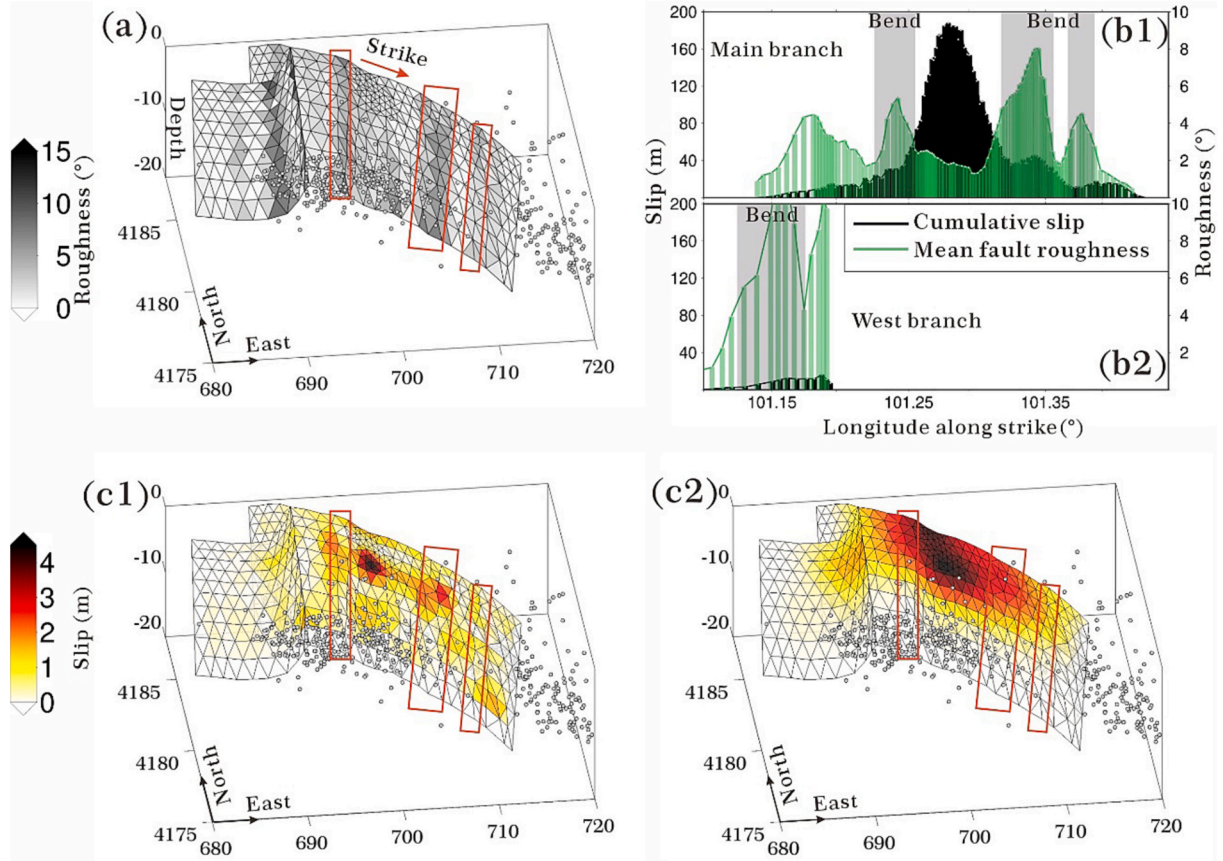


Fig. 7. Fault surface roughness. Red boxes in (a) and (c) show locations where the fault show substantial roughness, corresponding to the shaded areas in (b). (b1) and (b2) show fault slip (black, accumulated vertically) and correspondent mean fault surface roughness (green) at each location along the fault strike. (c1) and (c2) show an under-smoothed fault slip model (smoothing factor = 0) and an over-smoothed fault slip model (smoothing factor = 10), respectively. (For interpretation of the references to colour in this figure legend, the reader is referred to the web version of this article.)

the under-smoothed and the optimal models indicated that the latter captured the main features on the former and the main slip patch located in the middle of the two bends (highlighted by red boxes in Fig. 7). Some slipping patches on the under-smoothed model located right on the fault bend and the slip decreased dramatically outside the bend (i.e., away from the main slip patch). Despite a considerable degree of smoothing applied to the slip distribution, the phenomena of slip decreasing around the fault bends also persisted within the over-smoothed slip model (Fig. 7c2). These characteristics are consistent with the optimal slip model in Fig. 7b, all suggesting the impediment effect of fault bends acting on the slip propagation.

It should be noted that the above analysis, requiring a high-resolution slip distribution, is only possible when detailed fault geometry is available. Without such fault structural information, some of the faulting mechanisms such as the geometric transition of the aftershocks (Fig. 6c), the sharp slip drop near fault bends (Fig. 7b) and the overall slip propagation pattern would be hard to study. These coseismic rupture phenomena provide valuable opportunities to learn about the Earth's crust, future earthquake nucleation and the way faults are structured, especially the fault's maturity. Such accurate models and simulations of earthquake behavior can help engineers design structures to resist specific fault-related movements and significantly reduce earthquake damage and save lives (Freddi et al., 2021).

7. Conclusion

We have constructed a fault geometry of the 2022 Mw 6.7 Menyuan earthquake using triangular dislocations based on detailed fault surface fractures observed by optical images, SAR offsets and UAV measurements. The fault slip was modeled in an elastic half space constrained by InSAR phases and SAR offsets, accounting respectively for near- and far-field deformation. The triangular dislocation avoids discontinuities and overlaps at fault bends and step-overs so that the studies of the fault structure, stress interaction, and slip mechanics become possible.

The earthquake rupture was initiated on the previously mapped LLLF (the main branch) and forked southward to the TLSF at its western end (the west branch). The main branch accommodated most of the slip and the west branch accounted for ~13% of the rupture energy. Three clusters of aftershocks (Figs. 5a3 and 6c) were located which were all predicted by coseismic induced positive ΔCFS . The first two aftershock clusters (Fig. 6c1) likely shared a similar fault striking direction and distributed mostly parallel to the main branch but were shifted by ~4 km from each other due to a stress shadow at the western edge of cluster 1. Going further west close to the west fault branch, local faults related to the aftershocks gradually changed from EW striking to NS striking at a transition zone between clusters 2 and 3 (Fig. 6c2) as evidenced by the change of the induced stress direction.

The mechanism of fault branching can be explained by a releasing bend connecting the main and west branches (Fig. 6a) due to stronger strain localization than a northward branching (i.e., to the closely located SQF). The observed fault bends resulted in considerable slip surface roughness which caused sharp slip decreases by impeding slip propagation even before reaching the peak-rough patches and therefore largely controlled the slip magnitude and termination. The calculated fault plane roughness and its spatial variation reflects the maturity of the fault and these properties are important for the growth and nucleation of future earthquakes.

To conclude, such investigations of fault slip mechanics and aftershocks are benefited of a detailed fault structure constructed in this study, especially at fault step-overs, joints, and bends. This implies that the existence of unexplained aftershocks by positive ΔCFS or unexpected slip terminations of numerous previous earthquakes (e.g., Meade et al., 2017; Segou and Parsons, 2014; Storti et al., 2007) may be due to, if not entirely, the lack of detailed fault structural information which is worth re-investigating. With the advances of geodetic and geophysical observations, it is suggested that such analysis should be conducted routinely

for future large events and to uncover more properties of the Earth's shallow crust.

CRediT authorship contribution statement

Chen Yu: Writing – original draft, Visualization, Validation, Software, Methodology, Investigation, Formal analysis, Conceptualization. **Zhenhong Li:** Writing – review & editing, Supervision, Software, Resources, Project administration, Methodology, Funding acquisition, Conceptualization. **Chuang Song:** Writing – review & editing, Software, Methodology. **Bingquan Han:** Writing – review & editing, Software, Data curation. **Bo Chen:** Writing – review & editing, Software, Formal analysis. **Xinlong Li:** Writing – review & editing, Software, Formal analysis. **Jianbing Peng:** Writing – review & editing, Resources, Formal analysis, Conceptualization.

Declaration of competing interest

The authors declare that they have no known competing financial interests or personal relationships that could have appeared to influence the work reported in this paper.

Data availability

The Sentinel-1 interferograms and offsets, surface fractures identified by GF-7 and UAV, fault surface lines, and the fault slip model in the study are available at Harvard Dataverse via <https://doi.org/10.7910/DVN/TAEHK1> licensed under CC01.0 (public domain).

Acknowledgement

This research was funded by the National Natural Science Foundation of China (41941019), the Shaanxi Province Science and Technology Innovation Team (2021TD-51), the Shaanxi Province Geoscience Big Data and Geohazard Prevention Innovation Team (2022), and the Fundamental Research Funds for the Central Universities, CHD (300102263401, 300102260301, 300102261108, 300102262902, and 300203211261).

References

- Aiazzi, B., Baronti, S., Selva, M., Alparone, L., 2006. Enhanced Gram-Schmidt Spectral Sharpening Based on Multivariate Regression of MS and Pan Data. 2006 IEEE International Symposium on Geoscience and Remote Sensing, 31 July–4 Aug. 2006.
- Allen, C.R., Grantz, A., Brune, J.N., Clark, M.M., Sharp, R.V., Theodore, T.G., Wolfe, E. W., Wyss, M., 1968. The Borrego Mountain, California, earthquake of 9 April 1968: a preliminary report. *Bull. Seismol. Soc. Am.* 58 (3), 1183–1186. <https://doi.org/10.1785/bssa0580031183>.
- Anastasopoulos, I., Gazetas, G., Loli, M., Apostolou, M., Gerolymos, N., 2010. Soil failure can be used for seismic protection of structures. *Bull. Earthq. Eng.* 8 (2), 309–326. <https://doi.org/10.1007/s10518-009-9145-2>.
- Andrews, D.J., 1989. Mechanics of fault junctions. *J. Geophys. Res. Solid Earth* 94 (B7), 9389–9397. <https://doi.org/10.1029/JB094iB07p09389>.
- Ben-Zion, Y., Peng, Z., Okaya, D., Seeber, L., Armbruster, J.G., Ozer, N., Michael, A.J., Baris, S., Aktar, M., 2003. A shallow fault-zone structure illuminated by trapped waves in the Karadere–Duzce branch of the North Anatolian Fault, western Turkey. *Geophys. J. Int.* 152 (3), 699–717. <https://doi.org/10.1046/j.1365-246X.2003.01870.x>.
- Burov, E.B., Watts, A.B., 2006. The long-term strength of continental lithosphere: “Jelly sandwich” or “crème brûlée”? *GSA Today* 16 (1), 4–10. [https://doi.org/10.1130/1052-5173\(2006\)016<4:TLTSOC>2.0.CO;2](https://doi.org/10.1130/1052-5173(2006)016<4:TLTSOC>2.0.CO;2).
- Chen, W.-P., Molnar, P., 1977. Seismic moments of major earthquakes and the average rate of slip in Central Asia. *J. Geophys. Res.* 82 (20), 2945–2969. <https://doi.org/10.1029/jb082i020p02945>.
- Chen, C.W., Zebker, H.A., 2000. Network approaches to two-dimensional phase unwrapping: intractability and two new algorithms. *J. Opt. Soc. Am. A* 17, 401–414.
- Chester, F.M., Logan, J.M., 1986. Implications for mechanical properties of brittle faults from observations of the Punchbowl fault zone, California. *Pure Appl. Geophys.* 124 (1), 79–106. <https://doi.org/10.1007/BF00875720>.
- Comninou, M., Dundurs, J., 1975. The angular dislocation in a half space. *J. Elast.* 5 (3–4), 203–216. <https://doi.org/10.1007/BF00126985>.

- Cooke, M.L., Dair, L.C., 2011. Simulating the recent evolution of the southern big bend of the San Andreas fault, Southern California. *J. Geophys. Res. Solid Earth* 116 (B4). <https://doi.org/10.1029/2010JB007835>.
- Dawers, N.H., Anders, M.H., Scholz, C.H., 1993. Growth of normal faults: displacement-length scaling. *Geology* 21 (12), 1107–1110. [https://doi.org/10.1130/0091-7613\(1993\)021<1107:Gonfdl>2.3.Co;2](https://doi.org/10.1130/0091-7613(1993)021<1107:Gonfdl>2.3.Co;2).
- Duan, B., Oglesby, D.D., 2005. Multicycle dynamics of nonplanar strike-slip faults. *J. Geophys. Res. Solid Earth* 110 (B3). <https://doi.org/10.1029/2004JB003298>.
- Elliott, A.J., Oskin, M.E., Liu-Zeng, J., Shao, Y., 2015. Rupture termination at restraining bends: the last great earthquake on the Altyn Tagh Fault. *Geophys. Res. Lett.* 42 (7), 2164–2170. <https://doi.org/10.1002/2015GL063107>.
- Fan, L., Li, B., Liao, S., Jiang, C., Fang, L., 2022. High-precision relocation of the aftershock sequence of the January 8, 2022, MS6.9 Menyuan earthquake. *Earthq. Sci.* 35 (2), 138–145. <https://doi.org/10.1016/j.eqs.2022.01.021>.
- Farr, T.G., Rosen, P.A., Caro, E., Crippen, R., Duren, R., Hensley, S., Kobrick, M., Paller, M., Rodriguez, E., Roth, L., Seal, D., Shaffer, S., Shimada, J., Umland, J., Werner, M., Oskin, M., Burbank, D., Alsdorf, D.E., 2007. The shuttle radar topography mission. *Rev. Geophys.* 45 (2), RG2004. <https://doi.org/10.1029/2005RG000183>.
- Faulkner, D.R., Mitchell, T.M., Jensen, E., Cembrano, J., 2011. Scaling of fault damage zones with displacement and the implications for fault growth processes. *J. Geophys. Res. Solid Earth* 116 (B5). <https://doi.org/10.1029/2010JB007788>.
- Favalli, M., 2004. Digital elevation model construction from structured topographic data: the DEST algorithm. *J. Geophys. Res.* 109 (F4), F04004. <https://doi.org/10.1029/2004JF000150>.
- Feng, W., Samsonov, S., Qiu, Q., Wang, Y., Zhang, P., Li, T., Zheng, W., 2020. Orthogonal fault rupture and rapid postseismic deformation following 2019 Ridgecrest, California, earthquake sequence revealed from geodetic observations. *Geophys. Res. Lett.* 47 (5). <https://doi.org/10.1029/2019GL086888>.
- Fialko, Y., Sandwell, D., Agnew, D., Simons, M., Shearer, P., Minster, B., 2002. Deformation on nearby faults induced by the 1999 hector mine earthquake. *Science* 297 (5588), 1858–1862. <https://doi.org/10.1126/science.1074671>.
- Freddi, F., Galasso, C., Cremen, G., Dall'Asta, A., Di Sarno, L., Giaralis, A., Gutiérrez-Urzúa, F., Málaga-Chuquitaype, C., Mitoulis, S.A., Petrone, C., Sextos, A., Sousa, L., Tarbali, K., Tubaldi, E., Wardman, J., Woo, G., 2021. Innovations in earthquake risk reduction for resilience: recent advances and challenges. *Int. J. Disaster Risk Reduct.* 60, 102267. <https://doi.org/10.1016/j.ijdrr.2021.102267>.
- Fryer, B., Giorgetti, C., Passetlègue, F., Momeni, S., Lecampion, B., Violay, M., 2022. The influence of roughness on experimental fault mechanical behavior and associated microseismicity. *J. Geophys. Res. Solid Earth* 127 (8). <https://doi.org/10.1029/2022JB025113>. e2022JB025113.
- Fukahata, Y., Wright, T.J., 2008. A non-linear geodetic data inversion using ABIC for slip distribution on a fault with an unknown dip angle. *Geophys. J. Int.* 173 (2), 353–364. <https://doi.org/10.1111/j.1365-246X.2007.03713.x>.
- Gaudemer, Y., Tapponnier, P., Meyer, B., Peltzer, G., Shunmin, G., Zhitai, C., Huang, D., Cifuentes, I., 1995. Partitioning of crustal slip between linked, active faults in the eastern Qilian Shan, and evidence for a major seismic gap, the 'Tianzhu gap', on the western Haiyuan Fault, Gansu (China). *Geophys. J. Int.* 120 (3), 599–645. <https://doi.org/10.1111/j.1365-246X.1995.tb01842.x>.
- Griffith, W.A., Cooke, M.L., 2004. Mechanical validation of the three-dimensional intersection geometry between the Puente Hills blind-thrust system and the Whittier Fault, Los Angeles, California. *Bull. Seismol. Soc. Am.* 94 (2), 493–505. <https://doi.org/10.1785/0120030094>.
- Guo, N., Wu, Y., Zhang, Q., 2022. Coseismic and pre-seismic deformation characteristics of the 2022 MS 6.9 Menyuan Earthquake, China. *Pure Appl. Geophys.* 179 (9), 3177–3190. <https://doi.org/10.1007/s00024-022-03128-3>.
- Ha, G., Liu, J., Ren, Z., Zhu, X., Bao, G., Xu, D., Zhang, Z., 2022. The interpretation of seismogenic fault of the Madoi Mw 7.3 earthquake, Qinghai based on remote sensing images—a branch of the East Kunlun fault system. *J. Earth Sci.* 33 (4), 857–868. <https://doi.org/10.1007/s12583-021-1556-2>.
- Hanssen, R., 2001. *Radar Interferometry: Data Interpretation and Error Analysis*. Springer Science & Business Media.
- Harris, R.A., Segall, P., 1987. Detection of a locked zone at depth on the Parkfield, California, segment of the San Andreas Fault. *J. Geophys. Res. Solid Earth* 92 (B8), 7945–7962. <https://doi.org/10.1029/JB092iB08p07945>.
- He, P., Liu, C., Wen, Y., Hu, X., Ding, K., Xu, C., 2022. The 2022 Mw 6.6 Menyuan earthquake in the Northwest Margin of Tibet: geodetic and seismic evidence of the fault structure and slip behavior of the Qilian–Haiyuan Strike-Slip Fault. *Seismol. Res. Lett.* <https://doi.org/10.1785/0220220192>.
- Hu, X., Bürgmann, R., Schulz, W.H., Fielding, E.J., 2020. Four-dimensional surface motions of the Slumgullion landslide and quantification of hydrometeorological forcing. *Nat. Commun.* 11 (1), 2792. <https://doi.org/10.1038/s41467-020-16617-7>.
- Huang, Z., Zhou, Y., Qiao, X., Zhang, P., Cheng, X., 2022. Kinematics of the ~1000 km Haiyuan fault system in northeastern Tibet from high-resolution Sentinel-1 InSAR velocities: fault architecture, slip rates, and partitioning. *Earth Planet. Sci. Lett.* 583, 117450. <https://doi.org/10.1016/j.epsl.2022.117450>.
- Jackson, J., 2002. Strength of the continental lithosphere: time to abandon the jelly sandwich? *GSA Today* 12 (9), 4–10. [https://doi.org/10.1130/1052-5173\(2002\)012<0004:SOTCLT>2.0.CO;2](https://doi.org/10.1130/1052-5173(2002)012<0004:SOTCLT>2.0.CO;2).
- Jónsson, S.N., Zebker, H., Segall, P., Amelung, F., 2002. Fault slip distribution of the 1999 Mw 7.1 hector mine, California, earthquake, estimated from satellite radar and GPS measurements. *Bull. Seismol. Soc. Am.* 92 (4), 1377–1389. <https://doi.org/10.1785/0120000922>.
- Kaverina, A., Dreger, D., Price, E., 2002. The combined inversion of seismic and geodetic data for the source process of the 16 October 1999 Mw 7.1 hector mine, California, earthquake. *Bull. Seismol. Soc. Am.* 92 (4), 1266–1280. <https://doi.org/10.1785/0120000907>.
- Kilb, D., Gombert, J., Bodin, P., 2002. Aftershock triggering by complete Coulomb stress changes. *J. Geophys. Res. Solid Earth* 107 (B4). <https://doi.org/10.1029/2001JB000202>. ESE 2-1-ESE 2-14.
- Langridge, R.M., Stenner, H.D., Fumal, T.E., Christofferson, S.A., Rockwell, T.K., Hartleb, R.D., Bachhuber, J., Barka, A.A., 2002. Geometry, slip distribution, and kinematics of surface rupture on the Sakarya fault segment during the 17 August 1999 İzmit, Turkey, earthquake. *Bull. Seismol. Soc. Am.* 92 (1), 107–125. <https://doi.org/10.1785/0120000804>.
- Li, Z., Zhou, B., 2018. Influence of fault steps on rupture termination of strike-slip earthquake faults. *J. Seismol.* 22 (2), 487–498. <https://doi.org/10.1007/s10950-017-9719-4>.
- Li, Y.-G., Vidale, J.E., Aki, K., Xu, F., Burdette, T., 1998. Evidence of shallow fault zone strengthening after the 1992 M 7.5 landers, California, earthquake. *Science* 279 (5348), 217–219. <https://doi.org/10.1126/science.279.5348.217>.
- Li, Y.-G., Vidale, J.E., Cochran, E.S., 2004. Low-velocity damaged structure of the San Andreas Fault at Parkfield from fault zone trapped waves. *Geophys. Res. Lett.* 31 (12). <https://doi.org/10.1029/2003GL019044>.
- Li, C., Zhang, P.-Z., Yin, J., Min, W., 2009. Late Quaternary left-lateral slip rate of the Haiyuan fault, northeastern margin of the Tibetan Plateau. *Tectonics* 28 (5). <https://doi.org/10.1029/2008TC002302>.
- Li, Z., Han, B., Liu, Z., Zhang, M., Yu, C., Chen, B., Liu, H., Du, J., Zhang, S., Zhu, W., Zhang, Q., Peng, J., 2022. Source Parameters and Slip Distributions of the 2016 and 2022 Menyuan, Qinghai Earthquakes Constrained by InSAR Observations. *Geomatics and Information Science of Wuhan University*.
- Liu-Zeng, J., Yao, W., Liu, X., Shao, Y., Wang, W., Han, L., Wang, Y., Zeng, X., Li, J., Wang, Z., Liu, Z., Tu, H., 2022. High-resolution structure-from-motion models covering 160 km-long surface ruptures of the 2021 Mw 7.4 Madoi earthquake in northern Qinghai-Tibetan Plateau. *Earthq. Res. Adv.* 2 (2), 100140. <https://doi.org/10.1016/j.eqrea.2022.100140>.
- Luo, H., Wang, T., 2022. Strain partitioning on the Western Haiyuan fault system revealed by the adjacent 2016 Mw5.9 and 2022 Mw6.7 Menyuan earthquakes. *Geophys. Res. Lett.* 49 (16). <https://doi.org/10.1029/2022GL099348>. e2022GL099348.
- Maerten, F., Resor, P., Pollard, D., Maerten, L., 2005. Inverting for slip on three-dimensional fault surfaces using angular dislocations. *Bull. Seismol. Soc. Am.* 95 (5), 1654–1665. <https://doi.org/10.1785/0120030181>.
- Mann, P., Cunningham, W.D., Mann, P., 2007. Global catalogue, classification and tectonic origins of restraining- and releasing bends on active and ancient strike-slip fault systems. In: *Tectonics of Strike-Slip Restraining and Releasing Bends*, vol. 290. Geological Society of London, p. 0. <https://doi.org/10.1144/sp290.2>.
- Meade, B.J., 2007. Present-day kinematics at the India-Asia collision zone. *Geology* 35 (1), 81–84. <https://doi.org/10.1130/G22924A.1>.
- Meade, B.J., DeVries, P.M.R., Faller, J., Viegas, F., Wattenberg, M., 2017. What is better than Coulomb failure stress? A ranking of scalar static stress triggering mechanisms from 105 mainshock-aftershock pairs. *Geophys. Res. Lett.* 44 (22), 11,409–11,416. <https://doi.org/10.1002/2017GL075875>.
- Michel, R., Avouac, J.-P., Taboury, J., 1999. Measuring near field coseismic displacements from SAR images: application to the Landers Earthquake. *Geophys. Res. Lett.* 26 (19), 3017–3020. <https://doi.org/10.1029/1999GL000524>.
- Molnar, P., Lyon-Caen, H., 1989. Fault plane solutions of earthquakes and active tectonics of the Tibetan Plateau and its margins. *Geophys. J. Int.* 99 (1), 123–154. <https://doi.org/10.1111/j.1365-246X.1989.tb02020.x>.
- Nikkhoo, M., Walter, T.R., 2015. Triangular dislocation: an analytical, artefact-free solution. *Geophys. J. Int.* 201 (2), 1119–1141. <https://doi.org/10.1093/gji/ggv035>.
- Olson, E.L., Cooke, M.L., 2005. Application of three fault growth criteria to the Puente Hills thrust system, Los Angeles, California, USA. *J. Struct. Geol.* 27 (10), 1765–1777. <https://doi.org/10.1016/j.jsg.2005.02.005>.
- Pan, J., Li, H., Chevalier, M.-L., Tapponnier, P., Bai, M., Li, C., Liu, F., Liu, D., Wu, K., Wang, P., Li, C., Lu, H., Chen, P., 2022. Co-seismic rupture of the 2021, Mw7.4 Madoi earthquake (northern Tibet): short-cutting of the Kunlun fault big bend. *Earth Planet. Sci. Lett.* 594, 117703. <https://doi.org/10.1016/j.epsl.2022.117703>.
- Peng, H., Wang, J., Liu, C., Zhang, S., Niu, Y., Zhang, T., Song, B., Han, W., 2023. Mesozoic tectonothermal evolution of the Southern Central Asian Orogenic Belt: evidence from Apatite Fission-Track thermochronology in Shalazha Mountain, Inner Mongolia. *J. Earth Sci.* 34 (1), 37–53. <https://doi.org/10.1007/s12583-020-1053-z>.
- Sagy, A., Brodsky, E.E., Axen, G.J., 2007. Evolution of fault-surface roughness with slip. *Geology* 35 (3), 283–286. <https://doi.org/10.1130/g23235a.1>.
- Sathikumar, S., Barbot, S., 2021. The stop-start control of seismicity by fault bends along the Main Himalayan Thrust. *Commun. Earth Environ.* 2 (1), 87. <https://doi.org/10.1038/s43247-021-00153-3>.
- Sayab, M., Khan, M.A., 2010. Temporal evolution of surface rupture deduced from coseismic multi-mode secondary fractures: insights from the October 8, 2005 (Mw 7.6) Kashmir earthquake, NW Himalaya. *Tectonophysics* 493 (1), 58–73. <https://doi.org/10.1016/j.tecto.2010.07.001>.
- Segou, M., Parsons, T., 2014. The stress shadow problem in physics-based aftershock forecasting: does incorporation of secondary stress changes help? *Geophys. Res. Lett.* 41 (11), 3810–3817. <https://doi.org/10.1002/2013GL058744>.
- Shen, Z.-K., Sun, J., Zhang, P., Wan, Y., Wang, M., Bürgmann, R., Zeng, Y., Gan, W., Liao, H., Wang, Q., 2009. Slip maxima at fault junctions and rupturing of barriers during the 2008 Wenchuan earthquake. *Nat. Geosci.* 2 (10), 718–724. <https://doi.org/10.1038/ngeo0636>.
- Sone, H., Shimamoto, T., 2009. Frictional resistance of faults during accelerating and decelerating earthquake slip. *Nat. Geosci.* 2 (10), 705–708. <https://doi.org/10.1038/ngeo0637>.

- Song, C., Yu, C., Li, Z., Li, Y., Xiao, R., 2019. Coseismic slip distribution of the 2019 Mw 7.5 New Ireland earthquake from the integration of multiple remote sensing techniques. *Remote Sens.* 11 (23), 1–16. <https://doi.org/10.3390/rs11232767>.
- Storti, F., Salvini, F., Rossetti, F., Phipps Morgan, J., 2007. Intraplate termination of transform faulting within the Antarctic continent. *Earth Planet. Sci. Lett.* 260 (1), 115–126. <https://doi.org/10.1016/j.epsl.2007.05.020>.
- Tal, Y., Goebel, T., Avouac, J.-P., 2020. Experimental and modeling study of the effect of fault roughness on dynamic frictional sliding. *Earth Planet. Sci. Lett.* 536, 116133. <https://doi.org/10.1016/j.epsl.2020.116133>.
- Toda, S., Stein, R.S., Richards-Dinger, K., Bozkurt, S.B., 2005. Forecasting the evolution of seismicity in southern California: animations built on earthquake stress transfer. *J. Geophys. Res. Solid Earth* 110 (5), 1–17. <https://doi.org/10.1029/2004JB003415>.
- Wesnousky, S.G., 2006. Predicting the endpoints of earthquake ruptures. *Nature* 444 (7117), 358–360. <https://doi.org/10.1038/nature05275>.
- Westoby, M.J., Brasington, J., Glasser, N.F., Hambrey, M.J., Reynolds, J.M., 2012. 'Structure-from-Motion' photogrammetry: a low-cost, effective tool for geoscience applications. *Geomorphology* 179, 300–314. <https://doi.org/10.1016/j.geomorph.2012.08.021>.
- Xiao, L., Zheng, R., Zou, R., 2022. Coseismic slip distribution of the 2021 Mw7.4 Maduo, Qinghai earthquake estimated from InSAR and GPS measurements. *J. Earth Sci.* 33 (4), 885–891. <https://doi.org/10.1007/s12583-022-1637-x>.
- Xu, W., Feng, G., Meng, L., Zhang, A., Ampuero, J.P., Bürgmann, R., Fang, L., 2018. Transpressional rupture cascade of the 2016 Mw7.8 Kaikoura Earthquake, New Zealand. *J. Geophys. Res. Solid Earth* 123 (3), 2396–2409. <https://doi.org/10.1002/2017JB015168>.
- Yabuki, T., Matsu'ura, M., 1992. Geodetic data inversion using a Bayesian information criterion for spatial distribution of fault slip. *Geophys. J. Int.* 109 (2), 363–375. <https://doi.org/10.1111/j.1365-246X.1992.tb00102.x>.
- Ye, J., Liu, M., Wang, H., 2015. A numerical study of strike-slip bend formation with application to the Salton Sea pull-apart basin. *Geophys. Res. Lett.* 42 (5), 1368–1374. <https://doi.org/10.1002/2015GL063180>.
- Yin, A., Harrison, T.M., 2000. Geologic evolution of the Himalayan-Tibetan orogen. *Annu. Rev. Earth Planet. Sci.* 28 (1), 211–280.
- Yu, C., Li, Z., Penna, N.T.N.T., Crippa, P., 2018. Generic atmospheric correction model for interferometric synthetic aperture radar observations. *J. Geophys. Res. Solid Earth* 123 (10), 9202–9222. <https://doi.org/10.1029/2017JB015305>.
- Yuan, D.Y., Ge, W.P., Chen, Z.W., Li, C.Y., Wang, Z.C., Zhang, H.P., Zhang, P.Z., Zheng, D.W., Zheng, W.J., Craddock, W.H., Dayem, K.E., Duvall, A.R., Hough, B.G., Lease, R.O., Champagnac, J.D., Burbank, D.W., Clark, M.K., Farley, K.A., Garzone, C.N., Kirby, E., Molnar, P., Roe, G.H., 2013. The growth of northeastern Tibet and its relevance to large-scale continental geodynamics: a review of recent studies. *Tectonics* 32 (5), 1358–1370. <https://doi.org/10.1002/tect.20081>.
- Zhang, W., Jiao, D., Zhang, P., Molnar, P., Burchfiel, B.C., Deng, Q., Wang, Y., Song, F., 1987. Displacement along the Haiyuan Fault associated with the great 1920 Haiyuan, China, earthquake. *Bull. Seismol. Soc. Am.* 77 (1), 117–131.
- Zheng, A., Yu, X., Xu, W., Chen, X., Zhang, W., 2020. A hybrid source mechanism of the 2017 Mw 6.5 Jiuzhaigou earthquake revealed by the joint inversion of strong-motion, teleseismic and InSAR data. *Tectonophysics* 789, 228538. <https://doi.org/10.1016/j.tecto.2020.228538>.